

HPSTAR  
576-2018

# Evolution of a Novel Ribbon Phase in Optimally Doped $\text{Bi}_2\text{Sr}_2\text{CaCu}_2\text{O}_{8+\delta}$ at High Pressure and Its Implication to High- $T_C$ Superconductivity

Jianbo Zhang,<sup>†</sup> Yang Ding,<sup>\*,†</sup> Cheng-Chien Chen,<sup>§</sup> Zhonghou Cai,<sup>||</sup> Jun Chang,<sup>⊥</sup> Bijuan Chen,<sup>†</sup> Xinguo Hong,<sup>†</sup> Andrei Fluerașu,<sup>#</sup> Yugang Zhang,<sup>#</sup> Ching-Shun Ku,<sup>▽</sup> Dale Brewe,<sup>||</sup> Steve Heald,<sup>||</sup> Hirofumi Ishii,<sup>▽</sup> Nozomu Hiraoka,<sup>▽</sup> Ku-Ding Tsuei,<sup>▽</sup> Wenjun Liu,<sup>||</sup> Zhan Zhang,<sup>||</sup> Yong Q. Cai,<sup>#</sup> Genda Gu,<sup>○</sup> Tetsuo Irifune,<sup>◆,¶</sup> and Ho-kwang Mao<sup>†,∞</sup>

<sup>†</sup>Center for High-Pressure Science & Technology Advanced Research, Beijing, 100094, People's Republic of China

<sup>§</sup>Department of Physics, University of Alabama at Birmingham, Birmingham, Alabama 35294, United States

<sup>||</sup>Advanced Photon Source, Argonne National Laboratory, Argonne, Illinois 60439, United States

<sup>⊥</sup>College of Physics and Information Technology, Shaanxi Normal University, Xi'an 710119, People's Republic of China

<sup>#</sup>National Synchrotron Light Source II, Brookhaven National Laboratory, Upton, New York 11973, United States

<sup>▽</sup>National Synchrotron Radiation Research Center, Hsinchu 30076, Taiwan

<sup>○</sup>Condensed Matter Physics and Materials Science Department, Brookhaven National Laboratory, Upton, New York 11973, United States

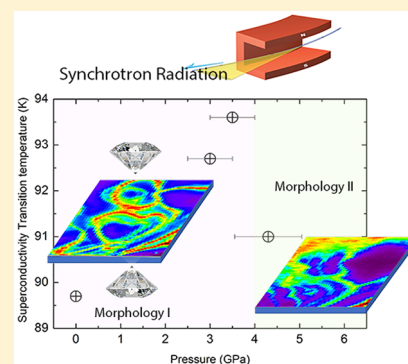
<sup>◆</sup>Geodynamics Research Center, Ehime University, 2–5 Bunkyo-cho, Matsuyama 790-8577, Japan

<sup>¶</sup>Earth-Life Science Institute, Tokyo Institute of Technology, Tokyo 152-8500, Japan

<sup>∞</sup>Geophysical Laboratory, Carnegie Institution of Washington, Washington, D.C. 20015, United States

## Supporting Information

**ABSTRACT:** One challenge in studying high-temperature superconductivity (HTSC) stems from a lack of direct experimental evidence linking lattice inhomogeneity and superconductivity. Here, we apply synchrotron hard X-ray nanoimaging and small-angle scattering to reveal a novel micron-scaled ribbon phase in optimally doped  $\text{Bi}_2\text{Sr}_2\text{CaCu}_2\text{O}_{8+\delta}$  (Bi-2212, with  $\delta = 0.1$ ). The morphology of the ribbon-like phase evolves simultaneously with the dome-shaped  $T_C$  behavior under pressure. X-ray absorption studies show that the increasing of  $T_C$  is associated with oxygen-hole redistribution in the  $\text{CuO}_2$  plan, while  $T_C$  starts to decrease with pressure when oxygen holes become immobile. Additional X-ray irradiation experiments reveal that nanoscaled short-range ordering of oxygen vacancies could further lower  $T_C$ , which indicates that the optimal  $T_C$  is affected not only by an optimal morphology of the ribbon phase, but also an optimal distribution of oxygen vacancies. Our studies thereby provide for the first time compelling experimental evidence correlating the  $T_C$  with micron to nanoscale inhomogeneity.



Optimal inhomogeneity has been regarded as crucial for achieving the maximal  $T_C$  in  $\text{YBa}_2\text{Cu}_3\text{O}_{6+y}$ <sup>1–6</sup> and other high-temperature superconductors,<sup>7–12</sup> which, however, lacks direct experimental evidence. Among different cuprate families,  $\text{Bi}_2\text{Sr}_2\text{CaCu}_2\text{O}_{8+\delta}$  (Bi-2212, with  $\delta = 0.1$ ) is one of the most studied systems for understanding inhomogeneity and its effects on the electronic structure.<sup>13</sup> The nanoscale electronic and topological inhomogeneity of Bi-2212 have been widely investigated for decades by many techniques, such as angular resolved X-ray photoemission and scanning tunneling electron microscopy.<sup>14–18</sup> However, direct experimental evidence linking structural inhomogeneity and  $T_C$  remain to be established, which hinders our understanding of the mechanism of high-temperature superconductivity (HTSC). Here, by

using hard X-ray synchrotron nanoimaging<sup>19,20</sup> and small-angle scattering techniques, we report a newly discovered micron-scaled ribbon phase coexisting with the main bulk structure in a Bi-2212 single crystal. We further apply pressure and strong X-ray irradiation to monitor how  $T_C$  responds to the evolution of the ribbon phase. These measurements serve as clean means to study the correlation between  $T_C$  and inhomogeneity without introducing any other chemical changes. By contrast, the commonly used doping methods would simultaneously

Received: June 13, 2018

Accepted: July 6, 2018

Published: July 6, 2018

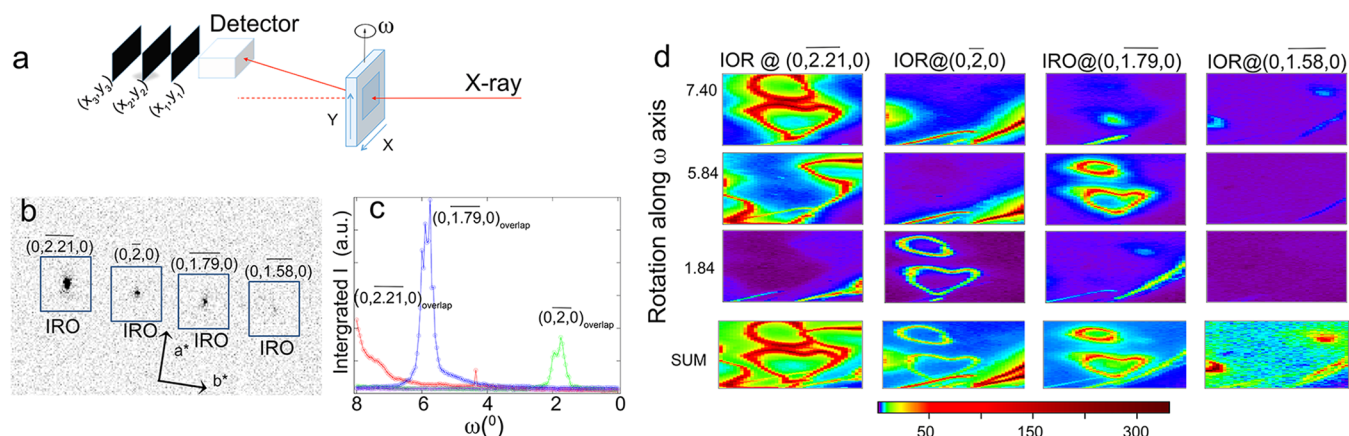


**Figure 1.** Contrast images from monochromatic submicron X-ray diffraction at 0.54 GPa. (a) Schematic experimental setup, where monochromatic X-ray of 20 keV is focused to  $\sim 0.4 \mu\text{m}$ , and a Pilatus detector is fixed with  $2\theta = 13^\circ$  in a horizontal scattering plane. (b) A typical diffraction pattern shows the (020) base peak and the accompanying modulation peaks. (c) Three additional diffraction peaks (from the ribbon phase) that overlap with the main peaks appear when the sample is rotated along the  $\omega$ -axis. (d) Contrast maps obtained from the ROI (range of interest) at three different angles, displaying a micrometre ribbon-like phase embedded in the modulated structure of single-crystal Bi-2212. The size of each map is  $40 \mu\text{m} \times 80 \mu\text{m}$  ( $V \times H$ ).

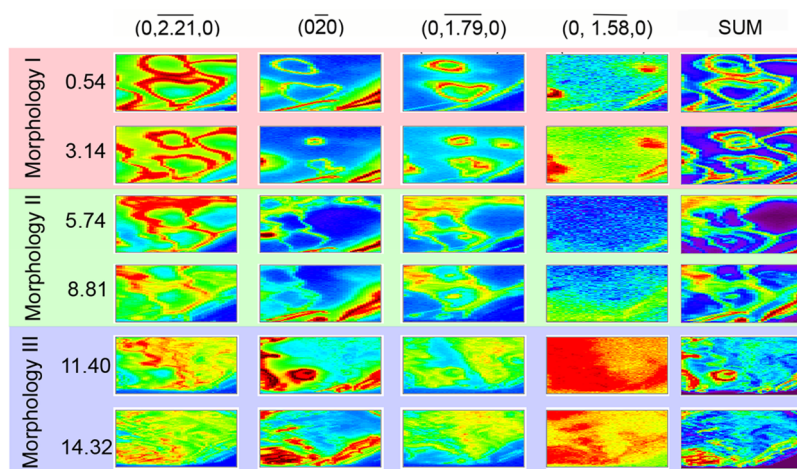


**Figure 2.** Contrast images for different diffraction peaks at various pressures and their sum. The morphology of the ribbon-like phase changes at three different stages: First, below 3.14 GPa, the ribbon-like pattern remains roughly the same, which is named as morphology phase I; Second, between 5.74 to 8.81 GPa, the ribbon-like phase appears to merge partially and the widths for some of the ribbons get broadened, which is denoted as morphology phase II. Finally, above 11.4 GPa, the ribbon-like phase widely disperses into the modulated structure, and they are no longer distinguishable from the contrast maps, which is morphology phase III. The maps in the last column are obtained by summing up the maps from different diffraction peaks. The size of each map is  $40 \mu\text{m} \times 80 \mu\text{m}$  ( $V \times H$ ).

change the chemistry, lattice inhomogeneity, and carrier concentration, thereby making it difficult to determine which parameter dominates the change of superconductivity. Our results not only reveal a direct link between optimal  $T_C$  and optimal inhomogeneity, but also demonstrate that hard-X-ray synchrotron nanoprobe could be a powerful tool to investigate lattice inhomogeneity and its implication to HTSC.

**Discovery of a Ribbon Phase in Bi-2212.** To disclose potential structure inhomogeneity in single-crystal samples and its evolution with pressure, we first apply the diffraction-contrast imaging technique, which is a typical method for transmission electron microscope and synchrotron X-ray. Figure 1 shows the X-ray diffraction measurements at 0.44 GPa, where a two-dimensional (2D) detector is placed at the Bragg angle of the  $(0, \bar{2}, 0)$  plane.<sup>21</sup> According to Bragg's law, in principle, only the  $(0, \bar{2}, 0)$  diffraction peak should be observed (Figure 1a). In actual experiments, however, there also exists three additional modulation peaks,  $(0, \bar{2.21}, 0)$ ,  $(0, \bar{1.79}, 0)$ , and

$(0, \bar{1.58}, 0)$ , as the thin sample would result in elongated diffraction rods in the reciprocal space. The elongated diffraction rods could be partially truncated by a 2D detector even away from the Bragg conditions,<sup>22</sup> similar to the zone-axis diffraction pattern from transmission electron microscopes. The observed  $0.21b^*$  incommensurate modulation has been commonly reported in Bi-2212 (Figure S-1c). Although its origin from either misfit strain<sup>18,21,23</sup> or excess oxygen dopant<sup>24</sup> is under debate, this lattice modulation has recently been associated with the modulation of superconducting gaps,<sup>14</sup> revealing the effect of specific lattice modulation on the superconducting  $\text{CuO}_2$  layers. Based on diffraction experiments, Castellan et al. have suggested that the modulation is associated with 2D domains in single-crystal samples, implying structural inhomogeneity in Bi-2212.<sup>25</sup>

When the sample is rotated about the  $\omega$ -axis from 0 to  $7.4^\circ$  (the limit of our high-pressure diamond anvil cell opening), we observe remarkably intense diffraction peaks  $(0, \bar{2.21}, 0)$ ,  $(0, \bar{2},$

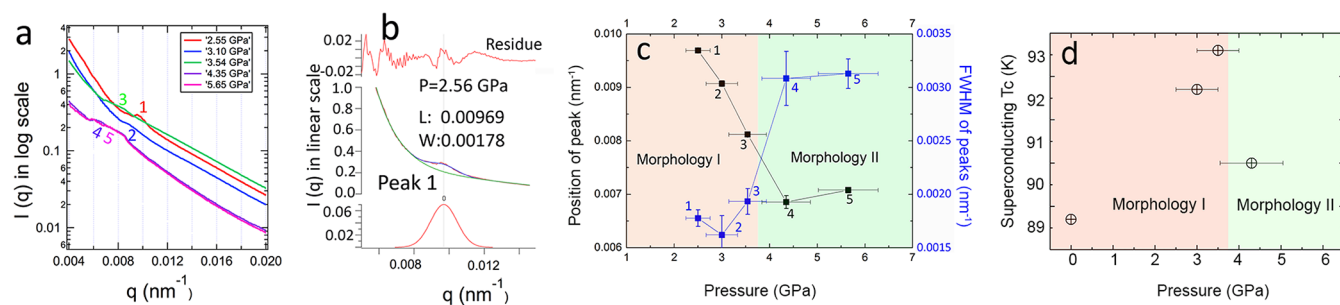


**Figure 3.** Results of small angle scattering measurements at high pressures. (a) Small-angle scattering intensity (in log scale) as a function of  $q$  measured at various pressures. The labeled peaks indicated in numeric form are caused by the presence of domains. (b) Peak-fitting of position ( $q$ ) and width of peak 1 (more details are shown in Figure S-4). (c) The pressure evolution of positions ( $q$ ) and widths for peaks 1, 2, 3, 4, and 5. Temperature-dependent electrical resistance  $R_{ab}$  of Bi-2212 single crystal up to 4.5 GPa as show in Figure S-3a, and the corresponding values of  $T_C$  are given in Table S-1. The plot indicates a critical transition pressure  $\sim 3.8$  GPa, which coincides with the pressure range of optimal  $T_C$  shown in panel d.

0), and  $(0, \bar{1}79, 0)$  at 7.4, 5.84, and  $1.84^\circ$ , respectively. These three peaks must arise from different domains or phases in the single-crystal Bi-2212 sample, whose diffraction peaks are overlapped with those from the main modulation phase. The domain structures revealed by the nanoimaging contrast maps are displayed in Figure 1d. Obtained from the ROI (region of interest) of the  $(0, \bar{2}21, 0)$  peak, the contrast map shows a micron-scale ribbon-like phase that intercalates with the modulated structure at 7.4 degrees. The ribbon phase has irregular closed-circle shapes with a width about 1–2  $\mu\text{m}$ . For the  $(0, \bar{1}79, 0)$  and  $(0, \bar{2}, 0)$  peaks, the contrast maps also show similar ribbon phases at 5.84 and  $1.84^\circ$  degrees, respectively. However, the maps from the  $(0, \bar{1}58, 0)$  peak do not show a ribbon morphology.

We note that the ribbon phase does not have a structural modulation, or otherwise the same phase would contribute to diffraction peaks overlapping with all the peaks at  $(0, \bar{2}21, 0)$ ,  $(0, \bar{2}, 0)$ ,  $(0, \bar{1}79, 0)$ , and  $(0, \bar{1}58, 0)$ , and it would appear in all the contrast maps simultaneously. Therefore, the ribbon-like pattern indicates a new phase distinct from the modulated structure of Bi-2212. The ribbons also have different orientations, as they appear at different angles. Furthermore, the ribbon phases observed at different angles do not interfere with each other, suggesting that they are spatially separated and exist at different depths along the crystal  $c$ -axis. These observations of the ribbon phase are consistent with the 2D domains in single-crystal Bi-2212 as suggested by Castellan et al.<sup>25</sup> X-ray fluorescence microscopy measurements (Figure S-2) have further confirmed that the ribbon phase is associated with lattice inhomogeneity, instead of fluctuation in the chemical composition of ions. Previous soft X-ray<sup>14–17</sup> and low-energy hard X-ray measurements in reflection geometry<sup>18</sup> failed to detect these phases, possibly due to limited probe penetration depth.

**Evolution of the Ribbon Phase with Pressure.** To study the overall morphology of the ribbons, we sum up the contrast maps of the same diffraction peak from all orientations into one contrast image, as shown in Figure 2. Below 3.14 GPa, the morphology and width of the ribbon remain; only the size of the circular shape reduces with increasing pressure. We name the morphology or ribbon phase in this pressure range as morphology I. From 5.74 to 8.81 GPa, the ribbon phase appears to merge partially and some of the ribbons broaden to 5–10  $\mu\text{m}$ , which is denoted as morphology II. When pressure exceeds 11.40 GPa, the ribbon phase widely spreads out into

the modulated structure, and they are no longer distinguishable from the contrast maps. We call the phase in morphology III. As the spatial resolution of the imaging experiment is about 1  $\mu\text{m}$ , information on nanoscale inhomogeneity is limited. We thereby further apply small-angle scattering to investigate possible submicron or nanoscale domains.

Figure 3a,b displays small-angle scattering results with X-ray beam parallel to the crystal  $c$ -axis. Peaks in the diffraction profile are associated with domain structures. In Figure 3c, the position of peak 1 is  $0.00969 \text{ nm}^{-1}$ , and its full width at half-maximum is  $0.00178 \text{ nm}^{-1}$ . The position and width respectively represent the averaged size  $\sim 2\pi/0.00969 \text{ nm} = 648 \text{ nm}$  and coherence length  $\sim 2\pi/0.00178 \text{ nm} = 3.5 \mu\text{m}$  of 2D domains in the  $ab$  plane at 2.55 GPa. At higher pressure, the domain size is increased roughly to 692 nm at 3.10 GPa, 768 nm at 3.54 GPa, and 917 nm at 4.54 GPa; it is then slightly decreased to 887 nm at 5.65 GPa. Meanwhile, the averaged coherence length is also increased roughly from 3.8  $\mu\text{m}$  at 3.10 GPa and to 3.9  $\mu\text{m}$  at 3.54 GPa, but it suddenly drops to  $\sim 2.0 \mu\text{m}$  at 4.35 and 5.65 GPa. The changes in domain size and coherence length with pressure show a clear critical transition pressure at  $\sim 3.8$  GPa, which is consistent with the morphology transition pressure of the ribbon phase.

Since both the imaging and scattering measurements have indicated a critical pressure around  $\sim 3.8$  GPa, and the ribbon phase is the only domain structure observed in imaging measurements, the ribbon phase is likely the main cause for the peaks observed in small-angle scattering. Although the width of the ribbon phase ( $\sim 1\text{--}2 \mu\text{m}$ ) is not exactly equivalent to the domain size ( $\sim 600\text{--}900 \text{ nm}$ ) in scattering measurements, the imaging technique has a spatial resolution  $\sim 1\text{--}2 \mu\text{m}$ , so it cannot resolve any submicron feature. This also explains why the ribbon width in imaging experiments always remains as 1–2  $\mu\text{m}$  below 3.14 GPa, since the actual ribbon width is smaller than the experimental resolution. On the other hand, the size of the domain keeps increasing in small-angle scattering measurements with pressure. We note that the change in morphology of the ribbon phase more precisely coincides with the change in coherence length of the domains above the optimal pressure at  $\sim 3.8$  GPa.

**Link between Optimal  $T_C$  and Optimal Inhomogeneity.** To further study the connection between superconductivity and the ribbon phase, we compare its morphological evolution and the corresponding change in  $T_C$  with pressure. As shown in Figure 3d, an intriguing coincidence exists: Below  $\sim 3.8$  GPa,

the morphology I of the ribbon phase stays, and  $T_C$  is enhanced from 89 to 93.6 K at a rate of  $\sim 1$  K/GPa. Above  $\sim 3.8$  GPa, the morphology II of the ribbons starts to change, and  $T_C$  drops to 91 K at a rate of  $\sim 3.25$  K/GPa.

To study how the electronic structure changes with pressure, we also measure Cu  $K$ -edge X-ray absorption (XAS) spectra with  $ab$ -plane light polarization at high pressure (Figure 4).

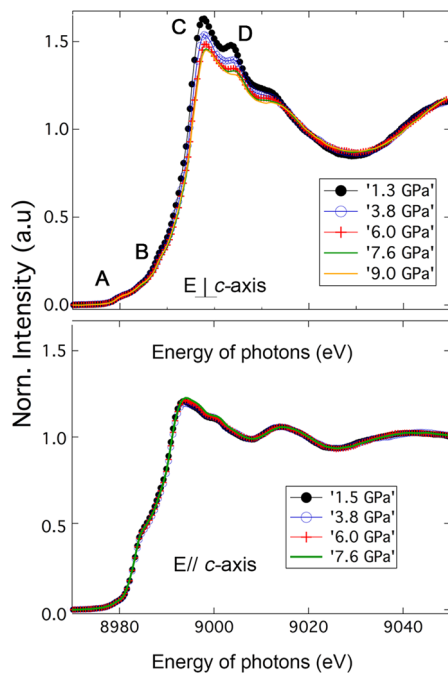


**Figure 4.** Cu  $K$ -edge X-ray absorption near-edge spectra on single-crystal Bi-2212 at high pressure with light polarization being normal to the  $c$ -axis [top panel] and parallel to the  $c$ -axis [bottom panel]. The spectra are normalized with the pre-edge constant backgrounds being subtracted. Peak A is related to Cu  $1s$  to  $3d$  quadruple transition, and its intensity does not change with pressure, showing that the Cu hole density remains the same at different pressure points. Peaks B and C–D are respectively due to multiple scatterings with La/Sr atoms and with oxygen in the square  $\text{CuO}_2$  planes. The decrease in peak C and D's intensity with pressure should result from a pressure-induced in-plane oxygen hole density redistribution. The results suggest that in morphology phase I, the increasing of  $T_C$  with pressure is associated with the redistribution of oxygen holes.

Peak A is related to Cu  $1s$  to  $3d$  quadruple transition, while Peaks B and C–D are due to respectively multiple scatterings with La/Sr atoms and with oxygen in the  $\text{CuO}_2$  planes.<sup>26</sup> As peak A does not change with pressure, the Cu hole density most likely remains the same in our measurements. Peaks C and D, however, decrease with pressure. This should result from hole density redistribution among the in-plane oxygen atoms, which dominates the increasing of  $T_C$  in morphology I. However, once pressure is above  $\sim 3.8$  GPa when the morphology changes from I to II, the oxygen holes stop changing, and  $T_C$  also starts to decrease.

From the above measurements, we could conclude that the optimal  $T_C$  of Bi-2212 must be closely tied to an optimal morphology of ribbon phase, i.e., morphology I, while oxygen holes are mobile in the  $\text{CuO}_2$  plane. The increasing of  $T_C$  with pressure in morphology I could be simply understood by an enhanced charge carrier density by compression. However, once the optimal inhomogeneity pattern or morphology is

altered by pressure above  $\sim 3.8$  GPa, the planar oxygen-hole density becomes immobile and  $T_C$  starts to decrease. To further investigate the impact of oxygen holes on HTSC, we study how  $T_C$  varies with oxygen vacancies at high pressure, by exposing strong X-ray irradiation on Bi-2212 to induce short-range oxygen ordering.<sup>27</sup>

Figure 5 shows ambient-pressure coherent imaging measurements on samples without and with X-ray irradiation. X-ray irradiation can cause nanoscale short-range ordering of oxygen vacancies.<sup>27</sup> Our transport measurements on the irradiated sample show that short-range oxygen vacancy ordering would

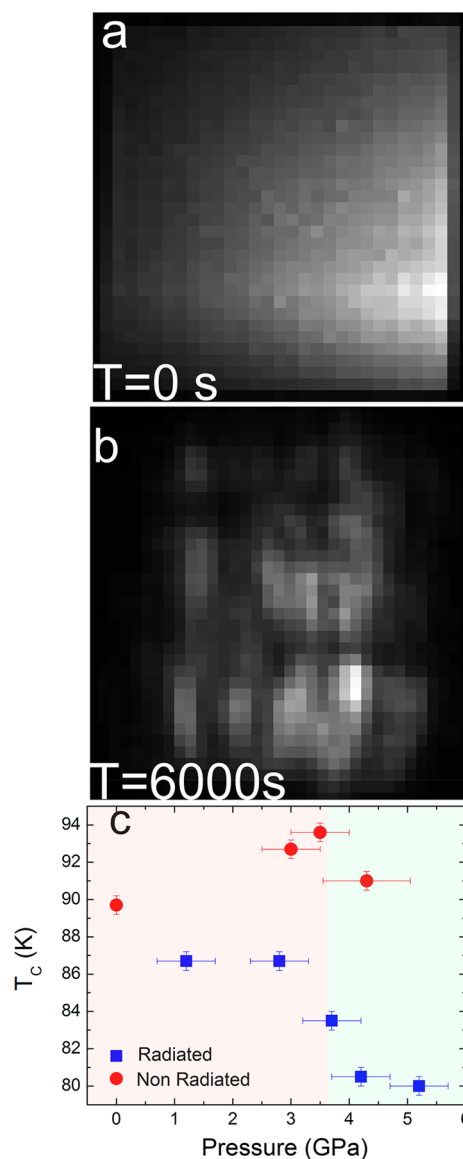


**Figure 5.** X-ray coherent imaging measurements on nonirradiated and irradiated Bi-2212 samples, and their  $T_C$  pressure evolution. (a) Coherent phase contrast image from single-crystal Bi-2212. (b) Coherent phase contrast image from Bi-2212 after 6000 s exposure to X-ray irradiation, which induces short-range nanoscale ordering. The size of the images is roughly  $90 \times 90$  nm<sup>2</sup>. (c)  $T_C$  as a function of pressure for (blue) Irradiated, (red) Non-irradiated samples. The values of  $T_C$  are listed in Table S-1 and also in Figure S-3. Nanoscale inhomogeneity of the radiated sample directly affects the  $T_C$ , but the optimal pressure occurs still in the range 3–4 GPa, where the ribbon phase starts to change its morphology.

lower  $T_C$  even if the Bi-2212 is in the optimal morphology I. This suggests that the optimal  $T_C$  is tied to not only an optimal morphology of ribbon phase, but also an optimal distribution of oxygen vacancies (or oxygen holes). Change in either of them will reduce the optimal  $T_C$ .

Although it remains challenging to make a conclusive statement about the origin of the ribbon phase, we speculate that the ribbon phase could originate from inhomogeneous ligand hole distribution, especially in an oxygen-poor regime, since it is not sensitive to X-ray irradiation (see discussion below) and low temperature.<sup>25</sup> The oxygen-poor ribbon phase and the oxygen-enriched regime form the conditions for granular superconductors. When pressure changes the inhomogeneity, the competition between pairing interaction and phase coherence then leads to a dome-shaped  $T_C$ .

Our results support the theoretical ideas of granular or percolative superconductivity and optimal inhomogeneity.<sup>28–31</sup> Granular superconductivity occurs when microscopic superconducting grains are separated by nonsuperconducting regions, while macroscopic superconductivity is established through Josephson tunneling between the grains.<sup>29</sup> For optimal inhomogeneity, inhomogeneous coupling could increase the pairing gap, but it would suppress the phase coherence above an optimal degree.<sup>32,33</sup>

Finally, we note that the critical pressure for achieving maximal  $T_C$  and the  $T_C$  itself both can vary with different Bi-2212 samples.<sup>34–36</sup> These results indicate that sample-specific and potentially material-specific inhomogeneity are strongly correlated with the behavior of superconductivity. Searching for optimal inhomogeneity could thereby be a key to designing new higher- $T_C$  compounds.

We have conclusively revealed a strong link between optimal  $T_C$  and optimal inhomogeneity involving the morphology of a newly discovered ribbon phase and the distribution of oxygen holes/vacancies in Bi-2212 single crystals. Therefore, our results provide compelling evidence to support the ideas of optimal inhomogeneity,<sup>28–33</sup> and challenge theories assuming only homogeneities in HTSC.

## MATERIALS AND METHODS

**Bi2212 Single Crystals.** The nearly optimally doped single crystals  $\text{Bi}_2\text{Sr}_2\text{CaCu}_2\text{O}_{8+\delta}$  (with  $\delta = 0.1$  and  $T_C = 91$  K at 1 bar) were grown by one of the coauthors (Genda Gu) with the conventional floating-zone technique and have been used in a number of previous studies.

**X-ray Diffraction Imaging Measurements.** The experiments were performed at sector 2-ID-D of the Advanced Photon Source, Argonne National Laboratory. Incident X-rays at 20 keV energy were focused down to  $\sim 0.4$   $\mu\text{m}$ . The sample was aligned with the  $c$ -axis nearly parallel to the incident X-ray beam. A 100 K Pilatus CCD detector was set at  $2\theta = 13$  degrees and 1.5 m away from the sample in a horizontal scattering plane. The data were taken at angles equal to 7.4, 5.84, and 1.84 degrees about the  $\omega$ -axis, respectively. For each collected set of data, the raster step size was set to 0.5  $\mu\text{m}$ . The diffraction contrast maps were generated by plotting the intensity of the diffraction peaks of interest as a function of its raster coordinates, where the X-ray diffraction data was taken. In the high-pressure measurements, single-crystal Bi-2212 was loaded with a ruby sphere (as a pressure standard) and Si oil (as a pressure transmission medium).

**High-Pressure Transport Measurements.** Electric resistance was measured with a standard four-probe-electrode circuit. A

T301 stainless steel gasket with cubic boron nitride/epoxy mixture powder inserts were used as a gasket. Si oil was used as a pressure medium, and a ruby scale was used to determine the pressure. Four thin gold probes were attached to the samples with silver glue for measuring the resistance.

**High-Pressure X-ray Absorption Measurements.** The high-pressure Cu  $K$ -edge X-ray absorption (XAS) measurements were performed at Sector 20 BM-B at Advanced Photon Source, Argonne National Laboratory. Single-crystal Bi-2212 samples were mounted in a pressure cell with nanocrystalline diamond anvils. The XAS spectra were measured in the total fluorescence yield mode, with a light polarization in the crystal  $a$ – $b$  plane. The XAS spectra were normalized with a standard procedure by subtracting the pre-edge constant backgrounds.

**X-ray Diffraction Small-Angle Scattering Measurements.** The experiments were performed at sector 11 coherent hard X-ray (CHX) beamline of NSLS-II, Brookhaven National Laboratory. Incident X-rays at 12.8 keV energy were focused down to  $\sim 0.5$   $\mu\text{m}$ . The single-crystal sample was aligned with the  $c$ -axis nearly parallel to the incident X-ray beam. A 4 M Eiger Pixel Array Detector was set at  $2\theta = 0$  degrees and 4 m away from the sample in a horizontal scattering plane. The data were taken by the pixel array detector with a beam-stop. For each collected set of data, the collection time was 900 s. The 1-D diffraction patterns were generated by integrating the intensity on the 2D detector as a function of scattering vector  $q$  ( $\text{nm}^{-1}$ ).

**Transmission Coherent Imaging Measurements.** The experiments were conducted on single-crystal Bi-2212 at ambient pressure at the X-ray Nanodiffraction beamline 21A of the Taiwan Photon Source (TPS) and some preliminary x-ray absorption, emission, resonant inelastic x-ray scattering study were also done at the beamline BL12XU/SPring-8 of National Synchrotron Radiation Research Center, Taiwan, National Synchrotron Radiation Research Center (NSRRC). A white X-ray beam with an energy range of 5–30 keV was used. The X-ray beams were focused to  $90 \times 90$  nm ( $H \times V$ ), and a Pilatus 100 K detector located at 4 m after focus point was used to collect coherent images.

## ASSOCIATED CONTENT

### Supporting Information

The Supporting Information is available free of charge on the ACS Publications website at DOI: 10.1021/acs.jpcllett.8b01849.

Additional details about the crystal structure of Bi-2212 with incommensurate modulation, chemical elemental mapping, temperature-dependent electrical resistance  $R_{ab}$  of nonirradiated and irradiated Bi-2212 single crystals at selected pressures, and peak fitting analysis of small-angle scattering experimental data (PDF)

## AUTHOR INFORMATION

### Corresponding Author

\*E-mail: yang.ding@hpstar.ac.cn.

### ORCID

Jianbo Zhang: 0000-0002-8339-1099

Steve Heald: 0000-0002-4369-8248

### Notes

The authors declare no competing financial interest.

## ACKNOWLEDGMENTS

The nanoimaging X-ray diffraction measurements were performed at sectors 2 ID-D of Advanced Photon Source, a U.S. Department of Energy (DOE) Office of Science user facility operated by Argonne National Laboratory (ANL) supported by the U.S. DOE Award No. DE-AC02-06CH11357. The coherent imaging experiments were performed at beamline 21A of Taiwan Photon Source, National Synchrotron Radiation Research Center, Taiwan. Y.D and H.-k.M. acknowledge the support from DOE-BES under Award No. DE-FG02-99ER45775 and NSFC Grant No. U1530402. Y.Q.C. and G.D.G. were supported by the U.S. Department of Energy, Office of Science, Office of Basic Energy Sciences, under Contract No. DE-SC0012704. This work is also supported by National Key R&D Program of China 2018YFA0305703 and the Science Challenge Project, No. TZ2016001. C.S.K acknowledge the support from MOST with Contract No. 106-2119-M-213-001-MY3.

## REFERENCES

- (1) Müller, P. Intrinsic Josephson Effects in Layered Superconductors. In *Festkörperprobleme 34; Advances in Solid State Physics*; Helbig, R., Ed.; Springer: Berlin Heidelberg, 1994; Vol. 34, p 1.
- (2) Fratini, M.; Poccia, N.; Ricci, A.; Campi, G.; Burghammer, M.; Aeppli, G.; Bianconi, A. Scale-free structural organization of oxygen interstitials in  $\text{La}_{(2)}\text{CuO}_{(4+y)}$ . *Nature* **2010**, *466*, 841–844.
- (3) Jorgensen, J. D.; Pei, S.; Lightfoot, P.; Shi, H.; Paulikas, A. P.; Veal, B. W. Time-dependent structural phenomena at room temperature in quenched  $\text{YBa}_2\text{Cu}_3\text{O}_{6.41}$ : Local oxygen ordering and superconductivity. *Phys. C* **1990**, *167*, 571.
- (4) Veal, B. W.; Paulikas, A. P.; You, H.; Shi, H.; Fang, Y.; Downey, J. W. Observation of temperature-dependent site disorder in  $\text{YBa}_2\text{Cu}_3\text{O}_{7-\delta}$  below 150 °C. *Phys. Rev. B: Condens. Matter Mater. Phys.* **1990**, *42*, 6305.
- (5) Ceder, G.; McCormack, R.; de Fontaine, D. Time-dependent oxygen ordering and its effect on Tc in off-stoichiometric  $\text{YBa}_2\text{Cu}_3\text{O}_x$ . *Phys. Rev. B: Condens. Matter Mater. Phys.* **1991**, *44*, 2377.
- (6) Friis Poulsen, H.; Hessel Andersen, N.; Vrtting Andersen, J.; Bohr, H.; Mouritsen, O. G. Relation between superconducting transition temperature and oxygen ordering in  $\text{YBa}_2\text{Cu}_3\text{O}_{6+x}$ . *Nature* **1991**, *349*, 594.
- (7) Geballe, T. H.; Marezio, M. Enhanced superconductivity in  $\text{Sr}_2\text{CuO}_{4-v}$ . *Phys. C* **2009**, *469*, 680.
- (8) Poccia, N.; Ricci, A.; Campi, G.; Fratini, M.; Puri, A.; Gioacchino, D. D.; Marcelli, A.; Reynolds, M.; Burghammer, M.; Saini, N. L.; et al. Optimum inhomogeneity of local lattice distortions in  $\text{La}_2\text{CuO}_{4+y}$ . *Proc. Natl. Acad. Sci. U. S. A.* **2012**, *109*, 15685.
- (9) Cooper, J. R. Scanning tunneling spectroscopy gap maps of cuprate single crystals: k-space anisotropy as an alternative to nanoscale inhomogeneity. *Phys. Rev. B: Condens. Matter Mater. Phys.* **2007**, *76*, 064509.
- (10) Hwu, Y.; Cheng, N. F.; Lee, S. D.; Tung, C. Y.; Alméras, P.; Berger, H. Chemical inhomogeneity and reactions of  $\text{BiSrCaCuO}$  surfaces detected by synchrotron imaging spectromicroscopy. *Appl. Phys. Lett.* **1996**, *69*, 2924.
- (11) Pan, S. H.; O'Neal, J. P.; Badzey, R. L.; Chamon, C.; Ding, H.; Engelbrecht, J. R.; Wang, Z.; Eisaki, H.; Uchida, S.; Gupta, A. K.; et al. Microscopic electronic inhomogeneity in the high-Tc superconductor  $\text{Bi}_2\text{Sr}_2\text{CaCu}_2\text{O}_{8+x}$ . *Nature* **2001**, *413*, 282.
- (12) Zeljkovic, I.; Nieminen, J.; Huang, D.; Chang, T. R.; He, Y.; Jeng, H. T.; Xu, Z.; Wen, J.; Gu, G.; Lin, H.; et al. Nanoscale interplay of strain and doping in a high-temperature superconductor. *Nano Lett.* **2014**, *14*, 6749–6753.
- (13) Saini, N. L.; Oyanagi, H.; Molle, M.; Garg, K. B.; Kim, C.; Bianconi, A. Evidence for anisotropic atomic displacements and orbital distribution in the inhomogeneous  $\text{CuO}_2$  plane of the  $\text{Bi}_2\text{Sr}_2\text{CaCu}_2\text{O}_{8+\delta}$  system. *J. Phys. Chem. Solids* **2004**, *65*, 1439–1443.
- (14) Slezak, J. A.; Lee, J.; Wang, M.; McElroy, K.; Fujita, K.; Andersen, B. M.; Hirschfeld, P. J.; Eisaki, H.; Uchida, S.; Davis, J. C. Imaging the impact on cuprate superconductivity of varying the interatomic distances within individual crystal unit cells. *Proc. Natl. Acad. Sci. U. S. A.* **2008**, *105*, 3203–3208.
- (15) Piriou, A.; Jenkins, N.; Berthod, C.; Maggio-Aprile, I.; Fischer, Ø. First direct observation of the Van Hove singularity in the tunnelling spectra of cuprates. *Nat. Commun.* **2011**, *2*, 221.
- (16) Parker, C. V.; Aynajian, P.; da Silva Neto, E. H.; Pushp, A.; Ono, S.; Wen, J.; Xu, Z.; Gu, G.; Yazdani, A. Fluctuating stripes at the onset of the pseudogap in the high-Tc superconductor  $\text{Bi}_2\text{Sr}_2\text{CaCu}_2\text{O}_{8+x}$ . *Nature* **2010**, *468*, 677.
- (17) Lawler, M. J.; Fujita, K.; Lee, J.; Schmidt, A. R.; Kohsaka, Y.; Kim, C. K.; Eisaki, H.; Uchida, S.; Davis, J. C.; Sethna, J. P.; et al. Intra-unit-cell electronic nematicity of the high-Tc copper-oxide pseudogap states. *Nature* **2010**, *466*, 347.
- (18) Poccia, N.; Campi, G.; Fratini, M.; Ricci, A.; Saini, N. L.; Bianconi, A. Spatial inhomogeneity and planar symmetry breaking of the lattice incommensurate supermodulation in the high-temperature superconductor  $\text{Bi}_2\text{Sr}_2\text{CaCu}_2\text{O}_{8+y}$ . *Phys. Rev. B: Condens. Matter Mater. Phys.* **2011**, *84*, 100504.
- (19) Ding, Y.; Cai, Z. H.; Hu, Q. Y.; Sheng, H. W.; Chang, J.; Hemley, R. J.; Mao, W. L. Nanoscale diffraction imaging of the high-pressure transition in  $\text{Fe}_{1-x}\text{O}$ . *Appl. Phys. Lett.* **2012**, *100*, 041903.
- (20) Libera, J.; Cai, Z.; Lai, B.; Xu, S. Integration of a hard x-ray microprobe with a diffractometer for microdiffraction. *Rev. Sci. Instrum.* **2002**, *73*, 1506.
- (21) Yamamoto, A.; Onoda, M.; Takayama-Muromachi, E.; Izumi, F.; Ishigaki, T.; Asano, H. Rietveld analysis of the modulated structure in the superconducting oxide  $\text{Bi}_2(\text{Sr,Ca})_3\text{Cu}_2\text{O}_{8+x}$ . *Phys. Rev. B: Condens. Matter Mater. Phys.* **1990**, *42*, 4228–4239.
- (22) Ding, Y.; Liu, H. Z.; Somayazulu, M.; Meng, Y.; Xu, J.; Prewitt, C. T.; Hemley, R. J.; Mao, H. Zone-axis x-ray diffraction of single-crystal  $\text{Fe}_{1-x}\text{O}$  under pressure. *Phys. Rev. B: Condens. Matter Mater. Phys.* **2005**, *72*, 174109.
- (23) Grebille, D.; Leligny, H.; Ruyter, A.; Labbe, P.; Raveau, B. Static Disorder in the Incommensurate Structure of the High Tc Superconductor  $\text{Bi}_2\text{Sr}_2\text{CaCu}_2\text{O}_{8+\delta}$ . *Acta Crystallogr., Sect. B: Struct. Sci.* **1996**, *52*, 628.
- (24) Petricek, V.; Gao, Y.; Lee, P.; Coppens, P. X-ray analysis of the incommensurate modulation in the 2:2:1:2 Bi-Sr-Ca-Cu-O superconductor including the oxygen atoms. *Phys. Rev. B: Condens. Matter Mater. Phys.* **1990**, *42*, 387–392.
- (25) Castellan, J. P.; Gaulin, B. D.; Dabkowska, H. A.; Nabialek, A.; Gu, G.; Liu, X.; Islam, Z. Two- and three-dimensional incommensurate modulation in optimally-doped  $\text{Bi}_2\text{Sr}_2\text{CaCu}_2\text{O}_{8+\delta}$ . *Phys. Rev. B: Condens. Matter Mater. Phys.* **2006**, *73*, 174505–174501.
- (26) Saini, N. L.; Lanzara, A.; Bianconi, A.; Oyanagi, H. Local structural features of the superconducting  $\text{Bi}_2\text{Sr}_2\text{CaCu}_2\text{O}_{8+\delta}$  system: A polarized Cu K-edge XAS study. *Phys. Rev. B: Condens. Matter Mater. Phys.* **1998**, *58*, 11768.
- (27) Poccia, N.; Fratini, M.; Ricci, A.; Campi, G.; Barba, L.; Vittorini-Orgeas, A.; Bianconi, G.; Aeppli, G.; Bianconi, A. Evolution and control of oxygen order in a cuprate superconductor. *Nat. Mater.* **2011**, *10*, 733–736.
- (28) Lang, K. M.; Madhavan, V.; Hoffman, J. E.; Hudson, E. W.; Eisaki, H.; Uchida, S.; Davis, J. C. Imaging the granular structure of high-Tc superconductivity in underdoped  $\text{Bi}_2\text{Sr}_2\text{CaCu}_2\text{O}_{8+\delta}$ . *Nature* **2002**, *415*, 412–416.
- (29) Phillips, J. C. Percolative theories of strongly disordered ceramic high temperature superconductors. *Proc. Natl. Acad. Sci. U. S. A.* **2010**, *107*, 1307–1310.
- (30) Kivelson, S. A.; Fradkin, E. *Handbook of High-Temperature Superconductivity: Theory and Experiment*; Springer: New York, 2007.
- (31) Poccia, N.; Lankhorst, M.; Golubov, A. A. Manifestation of percolation in high temperature superconductivity. *Phys. C* **2014**, *503*, 82–88.

(32) Arrigoni, E.; Kivelson, S. A. Optimal inhomogeneity for superconductivity. *Phys. Rev. B: Condens. Matter Mater. Phys.* **2003**, *68*, 180503.

(33) Giraldo-Gallo, P.; Zhang, Y.; Parra, C.; Manoharan, H. C.; Beasley, M. R.; Geballe, T. H.; Kramer, M. J.; Fisher, I. R. Stripe-like nanoscale structural phase separation in superconducting  $\text{BaPb}_{(1-x)}\text{Bi}_x\text{O}_3$ . *Nat. Commun.* **2015**, *6*, 8231.

(34) Klotz, S.; Schilling, J. S. Hydrostatic pressure dependence of the superconducting transition temperature to 7 GPa in  $\text{Bi}_2\text{Ca}_1\text{Sr}_2\text{Cu}_2\text{O}_{8+y}$  as a function of oxygen content. *Phys. C* **1993**, *209*, 499–506.

(35) Sen, P.; Bandyopadhyay, S. K.; Barat, P.; Mukherjee, P.; Mukhopadhyay, P. K.; De, A. The study of texturing of  $\text{Bi}_2\text{Sr}_2\text{CaCu}_2\text{O}_{8+\delta}$  and  $\text{Bi}_{1.84}\text{Pb}_{0.34}\text{Sr}_{1.91}\text{Ca}_{2.03}\text{Cu}_{3.06}\text{O}_{10+\delta}$  superconductors as a function of pelletisation pressure. *Phys. C* **1995**, *255*, 306.

(36) Chen, X. J.; Struzhkin, V. V.; Hemley, R. J.; Mao, H.-k.; Kendziora, C. High-pressure phase diagram of  $\text{Bi}_2\text{Sr}_2\text{CaCu}_2\text{O}_{8+\delta}$  single crystals. *Phys. Rev. B: Condens. Matter Mater. Phys.* **2004**, *70*, 214502.